J. Fluid Mech. (2009), *vol.* 621, *pp.* 103–130. © 2009 Cambridge University Press
doi:10.1017/S0022112008004655 Printed in the United Kingdom

Wake structure of a transversely rotating sphere at moderate Reynolds numbers

M. GIACOBELLO[1]†, A. OOI[2] AND S. BALACHANDAR[3]

[1]Air Vehicles Division, Defence Science and Technology Organisation, Fishermans Bend, Australia, 3207

[2]Department of Mechanical and Manufacturing Engineering, The University of Melbourne, Parkville, Melbourne, Australia, 3052

[3]Department of Mechanical and Aerospace Engineering, University of Florida, Gainesville, FL 32611, USA

(Received 23 July 2007 and in revised form 16 October 2008)

The uniform flow past a sphere undergoing steady rotation about an axis transverse to the free stream flow was investigated numerically. The objective was to reveal the effect of sphere rotation on the characteristics of the vortical wake structure and on the forces exerted on the sphere. This was achieved by solving the time-dependent, incompressible Navier–Stokes equations, using an accurate Fourier–Chebyshev spectral collocation method. Reynolds numbers Re of 100, 250 and 300 were considered, which for a stationary sphere cover the axisymmetric steady, non-axisymmetric steady and vortex shedding regimes. The study identified wake transitions that occur over the range of non-dimensional rotational speeds $\Omega^* = 0$ to 1.00, where Ω^* is the maximum velocity on the sphere surface normalized by the free stream velocity. At $Re = 100$, sphere rotation triggers a transition to a steady double-threaded structure. At $Re = 250$, the wake undergoes a transition to vortex shedding for $\Omega^* \geqslant 0.08$. With an increasing rotation rate, the recirculating region is progressively reduced until a further transition to a steady double-threaded wake structure for $\Omega^* \geqslant 0.30$. At $Re = 300$, wake shedding is suppressed for $\Omega^* \geqslant 0.50$ via the same mechanism found at $Re = 250$. For $\Omega^* \geqslant 0.80$, the wake undergoes a further transition to vortex shedding, through what appears to be a shear layer instability of the Kelvin–Helmholtz type.

1. Introduction

The sphere is arguably the most basic of three-dimensional geometries and serves as an excellent prototype for understanding the wake flow of more general bluff bodies. Engineering applications include combustion processes, particulate transport processes and atmospheric flows. Torobin & Gauvin (1960), among others, have noted that in these environments the streamwise rotation of particles is a far less common occurrence than transverse rotation. In the presence of a convection velocity, particle collisions with solid boundaries, collisions between particles moving at different convection velocities and streamwise velocity gradients, are more likely to induce rotation about an axis perpendicular to the flow direction.

In order to simulate particulate flows, Lagrangian simulation methods, which track the trajectories of a large number of particles, are often used. Here it is necessary to

† Email address for correspondence: matteo.giacobello@dsto.defence.gov.au

https://doi.org/10.1017/S0022112008004655 Published online by Cambridge University Press

be able to predict the forces to which the particles are exposed. Pan, Tanaka & Tsuji (2001) noted that data are still lacking for this purpose and were forced to assume a crude model for the lift force acting on particles in a rotating channel flow simulation. They stated that 'the lift force due to rotation of the particle for Reynolds numbers greater than 1.0 is still an open question.' Furthermore the particles may not behave simply as passive scalars but may work to actively modify the surrounding fluid flow. In some cases, vortex shedding from particles may have a significant effect on the enhancement of turbulence; so an understanding of the sphere wake structure is also of interest.

The uniform flow past a transversely rotating sphere is best known for a transverse aerodynamic force – often referred to as the Magnus effect – which leads to the deflection of its flight path. Rubinow & Keller (1961), by means of matched asymptotic expansions, derived an expression for the forces acting on a transversely rotating sphere for Reynolds numbers less than unity. They found the drag force to be independent of rotation and equal to the Stokes drag, while the lift force coefficient varied as $C_L = 2\Omega^*$. Here $\Omega^* = \Omega d/2U_\infty$ is the non-dimensional rotation rate; Ω is the angular velocity; d is the sphere diameter; and U_∞ is the free stream velocity magnitude. You, Qi & Xu (2003) computed the flow field for $Re = 0.5$ to 68.4 and $\Omega^* = 0$ to 5. At Reynolds numbers less than unity, the lift coefficient was found to be equal to the theoretical value reported by Rubinow & Keller (1961). For a given rotation rate, increasing the Reynolds number resulted in a monotonic decrease in the lift coefficient, such that it approached a constant value for $Re > 100$. Wake patterns computed for $Re = 34.2$ showed that increasing the rotation rate gradually reduced the size of the recirculating wake until it was completely destroyed.

The numerical study of Kurose & Komori (1999) considered $1 \leqslant Re \leqslant 500$ and $0 \leqslant \Omega^* \leqslant 0.25$. At $Re = 1$ they found a lift coefficient which was significantly lower than the value derived by Rubinow & Keller (1961) and computed by You *et al.* (2003). At higher Reynolds numbers they found that the rotation shifted the line of separation downstream on the low-pressure side of the sphere and upstream on the high-pressure side. For situations in which vortex shedding prevailed, the Strouhal number for vortex shedding was found to increase with an increasing rotation rate. The lift coefficient increased with the rotation rate. However, for a given rotation rate, the lift initially decreased with Reynolds number and then increased until it approached a constant value for $Re \geqslant 200$. The drag coefficient showed a monotonic increase with increasing rotation rate and decreasing Reynolds number.

Niazmand & Renksizbulut (2003) computed the flow field for $10 \leqslant Re \leqslant 300$ and $\Omega^* = 0$ to 1. For a Reynolds number well below the regular transition for a stationary sphere ($Re \approx 212$), rotation leads to an asymmetric wake, while symmetry is preserved about a plane normal to the rotation axis. With an increasing rotation rate, the recirculation zone becomes progressively smaller and is displaced to the high-pressure side of the sphere. At $Re = 100$ the wake was found to be suppressed for $\Omega^* \geqslant 0.5$. At Reynolds numbers approaching the regular transition for a stationary sphere, rotation can trigger a transition to vortex shedding. At $Re = 200$, time-periodic vortex shedding was attained for $\Omega^* \geqslant 0.5$. At Reynolds numbers approaching the Hopf bifurcation for a stationary sphere, lower rates of rotation are sufficient to trigger the transition to vortex shedding.

Early experimental investigations focused on relating the Reynolds number and rotation rate to the forces experienced by the sphere. At high Reynolds numbers, the sphere may be mounted in a wind tunnel via a spindle and driven by an electric

https://doi.org/10.1017/S0022112008004655 Published online by Cambridge University Press

motor mounted on a force balance (see for example Maccoll 1928). Tsuji, Morikawa & Mizuno (1985) emphasise that this method becomes inaccurate at moderate Reynolds numbers because the lateral force on the sphere is too small to be measured accurately and the sphere is small in relation to the support mechanism. As a result Tsuji *et al.* (1985) and Oesterlé & Dinh (1998) resorted to trajectory techniques, in which the flight path of a rotating sphere is measured, and the aerodynamic forces are recovered using momentum conservation equations. Although this avoids the inaccuracies of direct measurement, it introduces a host of other uncertainties. Tsuji *et al.* (1985) considered $Re = 550$ to 1600 and $\Omega^* < 0.70$. By assuming proportionality between the lift and rotation rate they found

$$C_L = (0.4 \pm 0.1)\,\Omega^*. \tag{1.1}$$

Oesterlé & Dinh (1998) considered $Re = 10$ to 140 and $\Omega^* = 1$ to 6. A best fit to their data gave the correlation

$$C_L \approx 0.45 + (2\Omega^* - 0.45)\exp(-0.075(\Omega^*)^{0.4}Re^{0.7}). \tag{1.2}$$

A much-needed experimental study of the wake flow came from Best (1998), who considered moderate Reynolds numbers in the range $Re = 29$ to 290 and rotation rates in the range $\Omega^* = 0$ to 1.5. Using an oil-filled recirculating channel, a suspension of fine particles was used for flow visualization and as seeding for velocity measurements, using laser doppler anemometry. The study considered the flow field on the two-dimensional streamwise plane normal to the rotation axis. For all Reynolds numbers considered, the mean wake length became progressively smaller with increasing rotation rate and ceased to exist when $\Omega^* > 0.5$. This transition is congruent with the wake suppression reported in the numerical studies of You *et al.* (2003) for $Re = 34.2$ and by Niazmand & Renksizbulut (2003) for $Re = 100$. For $\Omega^* < 0.5$, sphere rotation promoted a transition to unsteady vortex shedding, with a shedding frequency that was found to be modulated by the rotation rate. For $\Omega^* > 0.5$, fluid passing over the low-pressure side was dragged over the sphere lee side until it met fluid moving downstream over the high-pressure side of the sphere and was 'peeled off' the surface to form a shear layer. Unfortunately the experiment did not reveal the full three-dimensional nature of the wake.

Although a number of studies have considered the uniform flow past a transversely rotating sphere at moderate Reynolds numbers, the three-dimensional nature of the flow field and the mechanisms that drive the various wake transitions has not been previously explored. In this study, the wake structure of a spherical particle in steady rotation about an axis transverse to the free stream flow is investigated for the Reynolds numbers 100, 250 and 300. For a stationary sphere these cover the axisymmetric steady, non-axisymmetric steady and vortex shedding regimes. Non-dimensional rotation rates $\Omega^* = 0$ to 1 are considered. The numerical formulation is based on the schemes employed by Mittal (1999) and Bagchi & Balachandar (2002, 2003), except for the velocity boundary condition on the sphere surface and the details of the temporal discretisation. A detailed description of the numerical formulation is presented by Giacobello (2005), while the following section provides only a brief overview. Details of the wake structure are presented in increasing Reynolds number order in §§ 3.1–3.3, while the forces are presented in § 3.4.

https://doi.org/10.1017/S0022112008004655 Published online by Cambridge University Press

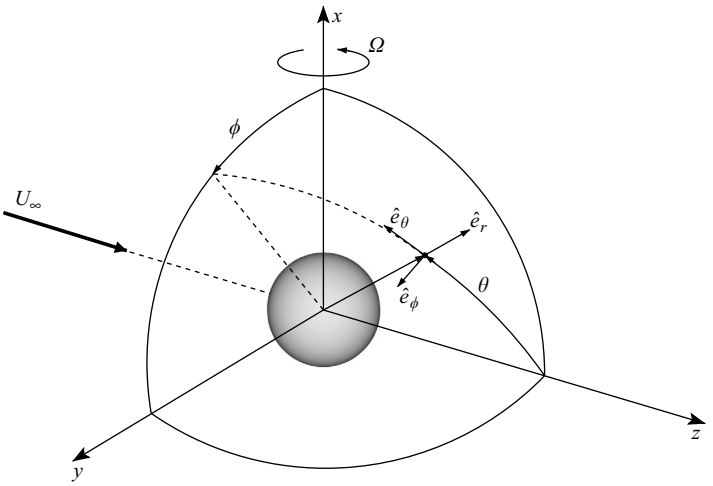


FIGURE 1. Problem geometry and coordinate system. The free stream flow is along the z-axis, and the sphere is constrained to rotate about the x-axis.

2. Numerical formulation

The fluid motion is fully described by the incompressible Navier–Stokes equations, which take the form

$$\frac{\partial \boldsymbol{u}}{\partial t} + \boldsymbol{u} \cdot \nabla \boldsymbol{u} = -\nabla P + \frac{1}{Re}\nabla^2 \boldsymbol{u} \tag{2.1}$$

and

$$\nabla \cdot \boldsymbol{u} = \boldsymbol{0}. \tag{2.2}$$

Here the Reynolds number, Re, is defined based on the free stream velocity U_∞, the diameter of the sphere d and the kinematic viscosity ν. The static pressure P is non-dimensionalized by the free stream dynamic pressure ρU_∞^2, where ρ is the fluid density. Equations (2.1) and (2.2) are solved directly for the primitive variables in a standard, spherical polar coordinate system, as defined in figure 1. The coordinate system comprises of a radial r, tangential θ and azimuthal direction ϕ, where

$$d/2 \leqslant r \leqslant D_o/2, \quad 0 \leqslant \theta \leqslant \pi \text{ and } 0 \leqslant \phi \leqslant 2\pi. \tag{2.3}$$

D_o is the diameter of the outer boundary of the computational domain. The unit vectors in the directions (r, θ, ϕ) are $(\widehat{\boldsymbol{e}}_{\boldsymbol{r}}, \widehat{\boldsymbol{e}}_{\boldsymbol{\theta}}, \widehat{\boldsymbol{e}}_{\boldsymbol{\phi}})$. A cartesian coordinate system, (x, y, z), is also introduced, such that the free stream flow vector is aligned with the positive z-axis and the sphere is constrained to rotate about the positive x-axis. The force coefficients in the z-, x- and y-direction are denoted C_D, C_{Lx} and C_{Ly} respectively. To aid the discussion, the sphere is divided into two hemispheres. The hemisphere over which the surface velocity has a component in the same direction as the free stream flow is referred to as the retreating side ($y > 0$); the hemisphere over which the surface velocity has a component in the direction opposite to the free stream flow is referred to as the advancing side ($y < 0$).

The equations are spatially discretized using a Fourier–Chebyshev collocation method that employs a restricted double Fourier series in the wall-parallel directions and a Chebyshev discretization in the wall-normal direction. The number of collocation points in the radial and tangential directions were $N_r = 121$ and $N_\theta = 100$ respectively. With increasing Re and Ω^* the number of collocation points in the

https://doi.org/10.1017/S0022112008004655 Published online by Cambridge University Press

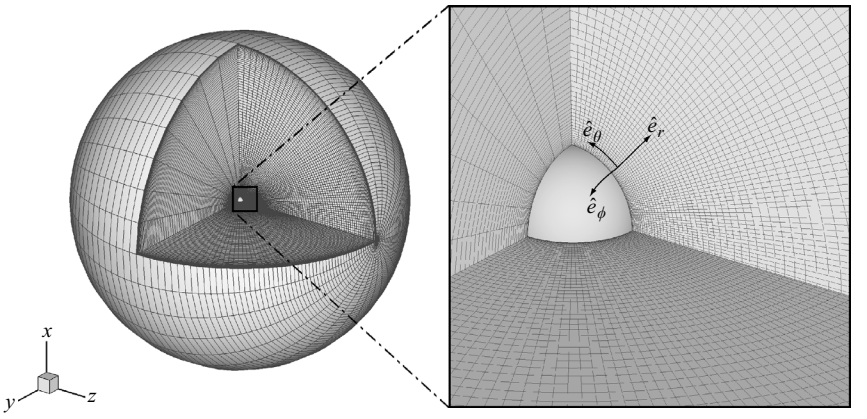


FIGURE 2. A representative computational grid. The collocation points are defined at the vertices of the cells.

azimuthal direction N_ϕ was varied from 16 to 64. For all simulations the outer boundary of the domain was truncated to $D_o = 45d$. A typical computational domain is presented in figure 2. A sector of the volume has been removed to show the distribution of collocation points through the domain. The magnified view shows the clustering of collocation points near the sphere surface and the wake region. The grid clustering in the near-wall region was tailored to ensure that at least 12 to 15 collocation points reside in the boundary layer, whereas clustering in the θ-direction was tailored to resolve the high gradients in the wake most efficiently.

The governing equations are time advanced using the fractional-step method described by Kim & Moin (1985) and a non-dimensional time step of $\Delta t^* = 0.0005$. The method recovers a second-order accurate velocity and pressure field. For all simulations, the primitive variables were initialized using a potential solution for the uniform flow past a stationary sphere. At non-dimensional time $t^* = 0$, the non-slip condition was applied to the sphere surface. With the exception of the velocity at the sphere surface, the initial and boundary conditions are detailed in Bagchi & Balachandar (2002). For a sphere rotating about the x-axis with a constant angular speed, the angular velocity vector is

$$\boldsymbol{\Omega} = \Omega(\sin\theta\cos\phi\,\hat{\boldsymbol{e}}_{\boldsymbol{r}} + \cos\theta\ \cos\phi\,\hat{\boldsymbol{e}}_{\boldsymbol{\theta}} - \sin\phi\,\hat{\boldsymbol{e}}_{\boldsymbol{\phi}}), \tag{2.4}$$

and the surface velocity distribution is

$$\boldsymbol{u}_s = \boldsymbol{\Omega} \times \left(\frac{d}{2}\hat{\boldsymbol{e}}_{\boldsymbol{r}}\right) = -\frac{\Omega d}{2}(\sin\phi\,\hat{\boldsymbol{e}}_{\boldsymbol{\theta}} + \cos\theta\cos\phi\,\hat{\boldsymbol{e}}_{\boldsymbol{\phi}}). \tag{2.5}$$

2.1. *Validation*

Insensitivity to spatial and temporal resolution was verified for all Reynolds numbers and rotation rates. Numerous preliminary simulations were undertaken to establish the most suitable grid parameters. The adequacy of the spatial and temporal resolution was verified by increasing the grid resolution and reducing the time step. It was confirmed that important parameters, such as the force coefficients, separation angle and shedding frequency, changed by less than 1 %. The spatial resolution was also assessed by transforming the velocity components into wavenumber space and monitoring the decay of the spectral modes (along the three coordinate directions)

https://doi.org/10.1017/S0022112008004655 Published online by Cambridge University Press

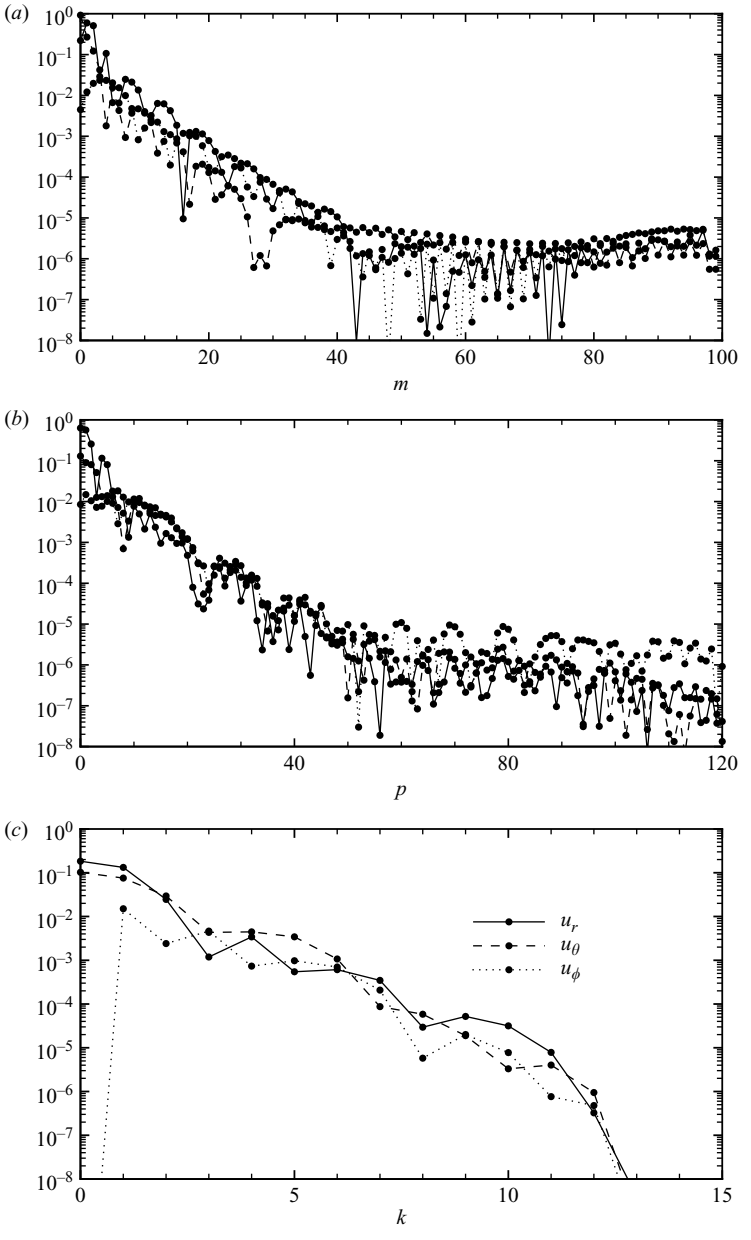


FIGURE 3. Instantaneous spectral modes of the spherical velocity components for $Re = 300$: (*a*) radial spectrum along $(\theta, \phi) = (0.056\pi, 0.188\pi)$; (*b*) tangential spectrum along $(r, \phi) = (1.92, 0.188\pi)$; (*c*) azimuthal spectrum along $(r, \theta) = (1.92, 0.056\pi)$.

with respect to the wavenumber. As an example, figure 3 presents instantaneous spectral modes versus the wavenumber at a grid point in the wake of a stationary sphere at $Re = 300$. Similar spectrums were calculated for each combination of r, θ and ϕ, and the grid resolution was judged to be adequate when at least four to five decades of decay in the expansion coefficients were maintained throughout the computational domain. A more detailed demonstration of the measures taken

https://doi.org/10.1017/S0022112008004655 Published online by Cambridge University Press

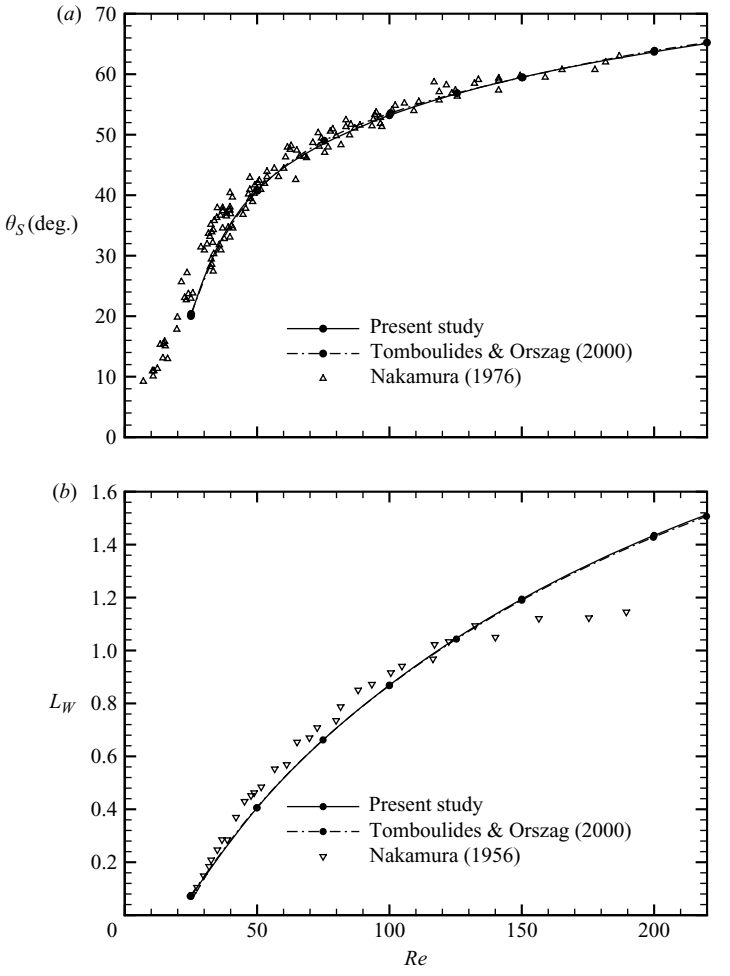


FIGURE 4. (*a*) Separation angle, θ_S, and (*b*) wake length, L_W, with respect to Re.

to ensure that each simulation was adequately resolved is presented in Giacobello (2005).

The solver was also validated against a range of experimental and numerical data for a stationary and rotating sphere in the Reynolds number range of interest. Here selected examples for a stationary sphere in the axisymmetric steady, non-axisymmetric steady and vortex shedding regimes are presented. This discussion also serves as a reference for the case in which sphere rotation is introduced.

In the range $Re = 20$ to 212, the uniform flow past a stationary sphere remains axisymmetric and steady and is characterized by a closed recirculating wake which is toroidal in structure. As the Reynolds number is increased in this regime the wake length and separation angle grow, while topologically the flow remains similar. Figure 4 presents the separation angle θ_S and wake length L_W with respect to the Reynolds number. Both the separation angle and the wake length are measured relative to the rear stagnation point, and the wake length is normalized by the sphere diameter. The results show close agreement with the values computed by Tomboulides & Orszag (2000), and extrapolation of the numerical data indicates

https://doi.org/10.1017/S0022112008004655 Published online by Cambridge University Press

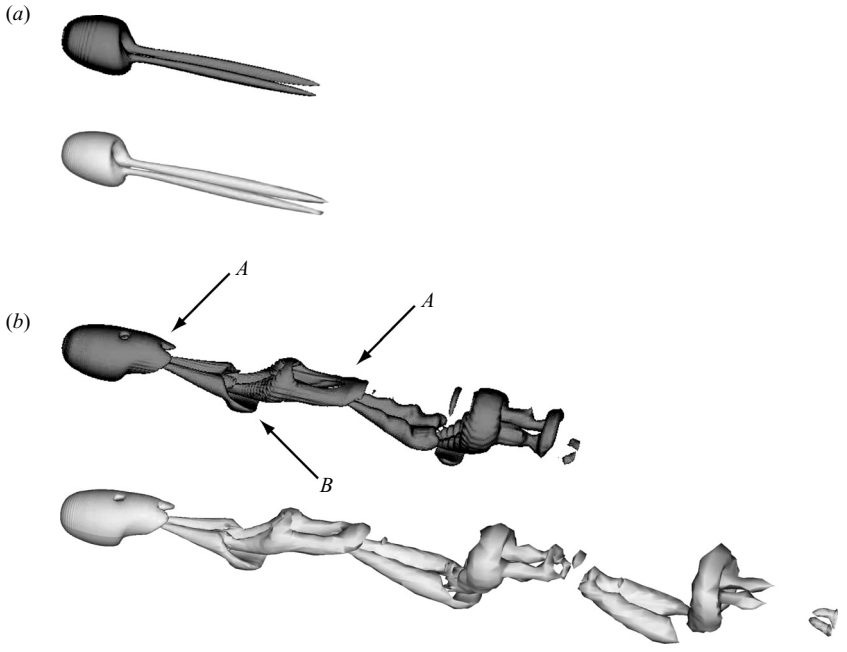


FIGURE 5. Vortical structures for a stationary sphere at (*a*) $Re = 250$; and (*b*) $Re = 300$. Structures are identified using the method of Jeong & Hussain (1995). Dark structures are the results of Kim & Choi (2002); light grey structures are the results of the present study, using a threshold value of $\lambda_2 = -8 \times 10^{-4}$.

separation to initially occur at a Reynolds number of about 20. The separation angles measured experimentally by Nakamura (1976) are also in close agreement at high Reynolds numbers but show higher values at the lower Reynolds numbers. The wake length measurements of Taneda (1956) are in agreement up to a Reynolds number of about 130. At Reynolds numbers above 130, Taneda (1956) reported faint periodic oscillations in the recirculating wake and, as noted by Tomboulides & Orszag (2000), this may be the cause of the discrepancy at higher Reynolds numbers.

Above the regular transition Reynolds number, the wake remains steady, but the toroidal vortex ring tilts off the streamwise axis. The shift in the vortex structure results in the azimuthal vorticity generated at the sphere surface having streamwise components that lead to the formation of two streamwise vorticity tails of equal strength and opposite signs. Although axisymmetry is lost, the flow field exhibits a symmetry plane passing between these vortical thread structures. This asymmetry results in a lateral lift force directed in the plane of symmetry. The wake no longer forms a closed structure, and fluid becomes entrained from upstream, spirals into the wake and is released into the two streamwise tails. In figure 5(*a*) the wake structure for $Re = 250$, as identified using the methods of Jeong & Hussain (1995), is compared with that computed by Kim & Choi (2002).

As the Reynolds number is increased in the non-axisymmetric steady regime, the streamwise vorticity tails strengthen and elongate until the wake undergoes a Hopf bifurcation at $Re \approx 270$. At higher Reynolds numbers planar symmetry is maintained, while the flow is characterized by the shedding of vortex loops, or hairpin vortices, at a single frequency. Figure 5(*b*) presents the instantaneous wake structure for

https://doi.org/10.1017/S0022112008004655 Published online by Cambridge University Press

	Re	$\overline{C_D}$	$\overline{C_L}$	St
Present study	250	0.702	0.061	
	300	0.658	0.067	0.134
Johnson & Patel (1999)	250		0.062	
	300	0.656	0.069	0.137
Constantinescu & Squires (2000)	250	0.700	0.062	
	300	0.665	0.065	0.136
Kim & Choi (2002)	250	0.702	0.060	
	300	0.657	0.067	0.134

TABLE 1. Comparison with earlier numerical results of the time-averaged drag coefficient $\overline{C_D}$, the lateral force coefficient $\overline{C_L}$ and the Strouhal number $St = fd/U_\infty$ where f is the frequency of vortex shedding.

$Re = 300$. Hairpin vortices are periodically shed from the sphere surface with the same orientation and sign (labelled A). The one-sided shedding also leads to a net lift force that acts along the plane of symmetry. There is also the appearance of induced vortices which are of opposite sign and orientation to those of the vortices shed from the sphere (labelled B). The induced structures were first observed by Johnson & Patel (1999), and they argued that they arise from an interaction of the near wake and the outer flow. Good agreement is evident with the result computed by Kim & Choi (2002). Table 1 compares the force coefficients and shedding frequencies for $Re = 250$ and $Re = 300$ with the numerical results reported by Johnson & Patel (1999), Constantinescu & Squires (2000) and Kim & Choi (2002). All values computed in the present study are within 3 % of those computed in these earlier simulations.

3. The flow past a transversely rotating sphere

3.1. $Re = 100$

Figure 6(a) presents the flow structure at $Re = 100$ for a number of representative rotation rates. In this and subsequent figures, the vortex identification method of Jeong & Hussain (1995) is used, and a threshold value of $\lambda_2 = -8 \times 10^{-4}$ is chosen. To indicate length scale, the wake cross-sections are marked at streamwise increments of $\Delta z = 2$, starting at $z = 0$. At this Reynolds number the wake remains steady over the range of Ω^* considered. For a stationary sphere, the flow topology comprises a shroud over the sphere and a torus in the near wake. This wake flow is described in some detail by Johnson & Patel (1999). The torus in the near wake coincides with the axisymmetric toroidal wake found at this Reynolds number, while, as noted by Johnson & Patel (1999), the shroud over the sphere does not coincide with any apparent vortical structure. However, they showed that in a coordinate system translating with the local velocity, closed streamline orbits coincide with the position of the shroud.

The introduction of sphere rotation forces the wake to undergo a transition to a double-threaded structure, similar to that found for a stationary sphere above the regular transition ($212 < Re < 270$). At $\Omega^* = 0.05$, the double threads exist but are comparatively weak and are not detected at the threshold value of λ_2 presented. Sphere rotation also distorts the shroud enveloping the sphere, causing it to grow over the advancing side and diminish over the retreating side of the sphere. With

https://doi.org/10.1017/S0022112008004655 Published online by Cambridge University Press

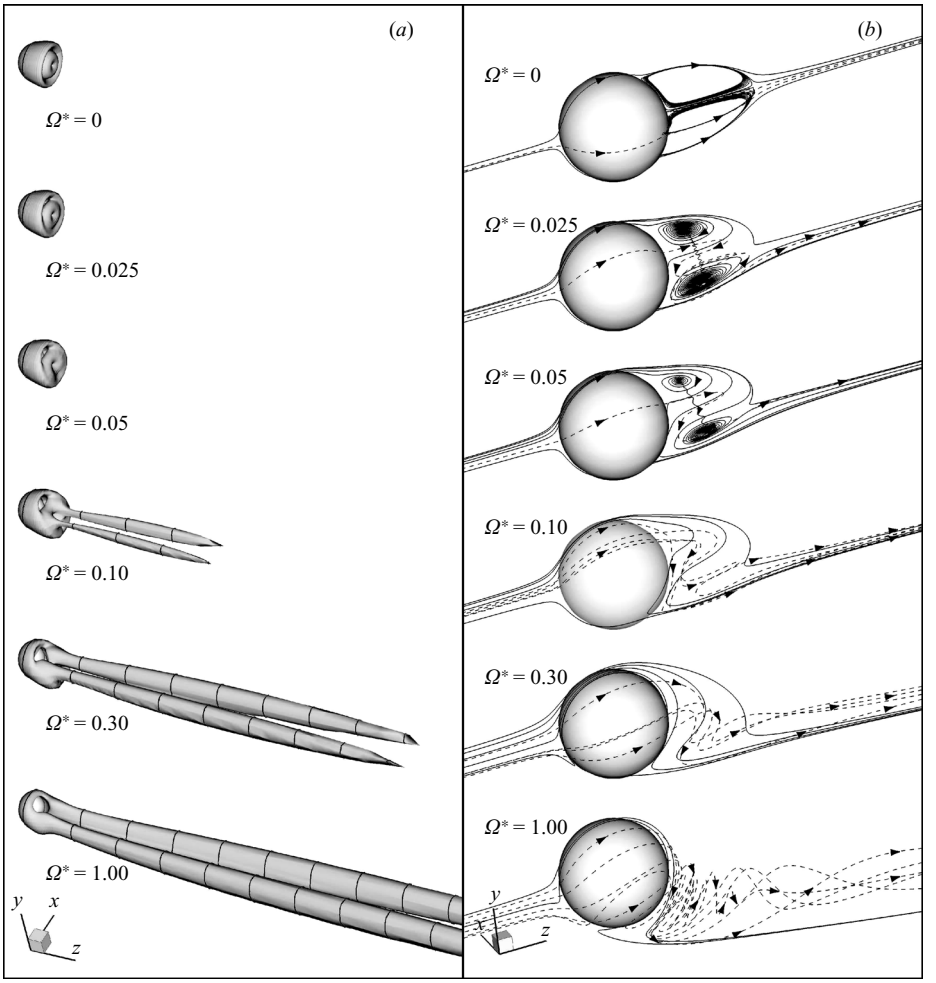


FIGURE 6. (*a*) Vortical structures and (*b*) three-dimensional streamline patterns for $Re = 100$.

increasing Ω^* the threads become thicker and elongated in the streamwise direction, indicating an increase in their rotational strength. The threads are also deflected in the negative y-direction as a result of the induced velocity of one tail on the other. Momentum conservation indicates that the deflection of the wake is accompanied by a lift or Magnus force in the positive y-direction.

The corresponding instantaneous streamlines are shown in figure 6(*b*). For clarity, only a few streamline paths are shown, and because the flow remains symmetric about the (y, z)-plane, only $x \geqslant 0$ is considered. For a stationary sphere the wake streamlines form concentric loops. A separatrix stream surface divides fluid within the toroidal wake from the outer flow. The introduction of sphere rotation breaks the flow axisymmetry, and the toroidal wake becomes tilted; however, over the range of $\Omega = 0$ to 1.00 the flow does maintain a plane of symmetry normal to the rotation axis. For $\Omega = 0.025$ and 0.05, fluid passing over the retreating side of the sphere is entrained into the wake and is ejected from the advancing side of the sphere. For convenience, the foci on the retreating and advancing sides of the wake will be referred to as the upper and lower foci, respectively; however, it is emphasized that they comprise part

https://doi.org/10.1017/S0022112008004655 Published online by Cambridge University Press

of a single three-dimensional toroidal structure. Fluid entrained into the wake from the retreating side spirals towards the stable upper focus and is ejected normal to the (y, z)-plane from its centre. Fluid then spirals azimuthally around the wake and feeds the unstable lower focus, before spiralling radially outwards from its centre and being released into the wake in two streams on either side of the symmetry plane. This wake structure is similar to that described by Johnson & Patel (1999) for a stationary sphere above the regular transition.

At $\Omega^* = 0.10$, the focal structures seen at lower rotation rates lose their spiral appearance in a stationary reference frame. As the rotation rate is increased further, the near wake becomes increasingly vectored in the negative y-direction, and fluid passing over the retreating side remains attached until it meets fluid passing over the advancing side of the sphere and is 'peeled off' to form a shear layer. Sphere rotation also causes a thin layer of fluid to rotate with the sphere surface (not shown). As the rotation rate increases this layer of fluid becomes progressively thicker. On the symmetry plane, the forward separatrix is shifted away from the surface and towards the advancing side of the sphere.

For $\Omega^* = 0.10$, the toroidal wake structure is barely discernible, while at the higher rotation rates it is absent. Both the numerical study of Niazmand & Renksizbulut (2003) and the experimental study of Best (1998) report the recirculating wake to be totally absent for $\Omega^* \geqslant 0.50$. At these higher rotation rates, fluid passing over the retreating side of the sphere is accelerated over the lee side of the sphere in a contracting band, while fluid passing over the advancing side forms a sheet that curls at its edges. These motions combine to form a pair of counter-rotating vortical structures, similar to those found downstream of a finite length wing. It is these counter-rotating vortical structures that are identified in figure 6(*a*) as intense streamwise threads.

The existence of a trailing vortex pair is not surprising, since, for a three-dimensional body that is generating lift, the laws of inviscid vortex motion dictate that trailing vortices must exist. The presence of a pair of counter-rotating vortical threads has been previously reported by Maccoll (1928) for a much higher Reynolds number ($Re > 10^4$). Using a three-component pressure gauge, Maccoll measured the time-averaged flow direction and speed over a number of cross-stream planes downstream of a sphere mounted in a wind channel. Calculated streamwise vorticity contours indicated the presence of a pair of vortex cores that were deflected towards the advancing side of the sphere.

3.2. $Re = 250$

The effect of sphere rotation on the flow structure at $Re = 250$ is illustrated in figure 7. For a stationary sphere, the wake comprises a double-threaded structure, which has been previously observed in both experiments and numerical simulations. These tails consist of streamwise vorticity, equal in magnitude and opposite in sign. It is through these tails that fluid entrained into the near wake is released downstream. The introduction of sphere rotation causes the tails to become elongated in the streamwise direction, as was also observed for $Re = 100$. However, above a critical value of the rotation rate, the wake undergoes a transition to an unsteady vortex shedding regime. This transition occurs at approximately $\Omega^* = 0.08$. Simulation at this non-dimensional rotation rate shows small amplitude wake oscillations with a slow decay rate, indicating that the flow is in the vicinity of a bifurcation between a steady regime and an unsteady regime. In figure 7 the instantaneous wake structure is presented for $t^* = 256.15$. The simulation was continued to $t^* = 600$, by which time the wake settles to a steady double thread. At higher rotation rates, the wake undergoes

https://doi.org/10.1017/S0022112008004655 Published online by Cambridge University Press

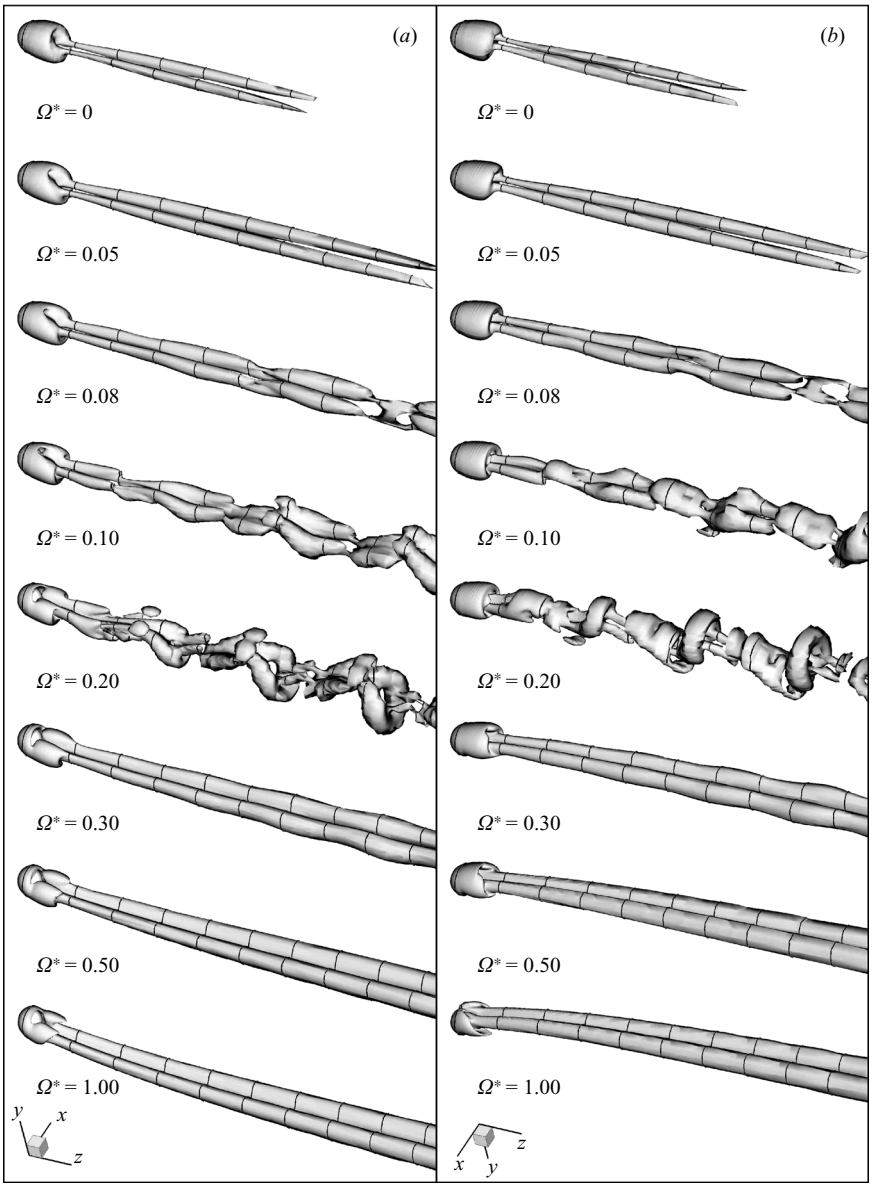


FIGURE 7. Instantaneous vortical structures for $Re = 250$: (*a*) and (*b*) look down on the wake from the retreating and advancing side of the sphere, respectively.

sustained vortex shedding. In this and subsequent figures that present a periodic wake, the time instant shown coincides with the lateral lift force being at a local minimum. With increasing Ω^*, the expansion of the wake in the y-direction increases before decreasing again, such that for $\Omega^* \geqslant 0.30$ vortex shedding is suppressed, and the wake reverts to the double-threaded structure. Some waviness is seen in the streamwise threads for $\Omega^* = 0.30$, while the wake is steady at higher Ω^*. At this Reynolds number Niazmand & Renksizbulut (2003) also reported a periodic wake for $\Omega^* > 0.05$; however they found this to persist up to the maximum rotation rate tested ($\Omega^* = 0.50$).

https://doi.org/10.1017/S0022112008004655 Published online by Cambridge University Press

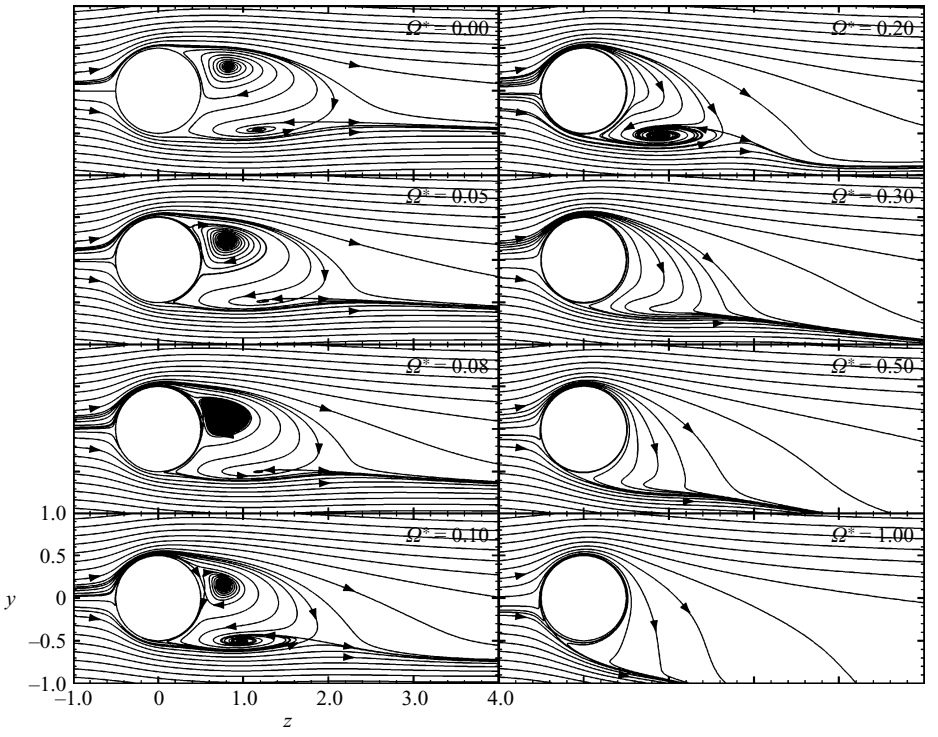


FIGURE 8. Instantaneous near-wake streamline patterns on the (y, z)-plane for $Re = 250$.

Figure 8 presents the near-wake streamline patterns on the symmetry plane for $Re = 250$. For unsteady cases, the patterns were obtained by numerically integrating the instantaneous velocity field in pseudo-time. These instantaneous streamlines serve only to describe the velocity field at an instant in time. It must be recognized that fluid that appears to be channelled along paths prescribed by the instantaneous streamlines may at some later instant follow a distinctly different path. The issue of correctly interpreting streamline patterns in unsteady flows is discussed at length by Steiner (1984).

For a stationary sphere at $Re = 250$ ($\Omega^* = 0$), the wake exists in a steady non-axisymmetric regime. Although axisymmetry is lost, the wake maintains a plane of symmetry, which coincides with the (y, z)-plane in the present simulations. This wake structure has been described in detail by Johnson & Patel (1999). Fluid passing over the upper side of the sphere is entrained into the wake, encircles the upper focus and spirals radially inwards towards the centre of the lower stable focus, before being expelled normal to the plane. It then spirals azimuthally along the vortex core and feeds into the centre of the unstable upper focus. This entrained fluid then spirals radially outwards and is sent around the lower focus before being released downstream.

The introduction of sphere rotation displaces the wake foci towards the negative y-direction, with the region of circulation around the upper focus becoming progressively smaller, such that it is absent for $\Omega^* \geqslant 0.20$. At $\Omega^* = 0.08$ the appearance of the upper focus changes from topologically stable to unstable. This shift in topology coincides with a transition to the vortex shedding regime. The circulation region

https://doi.org/10.1017/S0022112008004655 Published online by Cambridge University Press

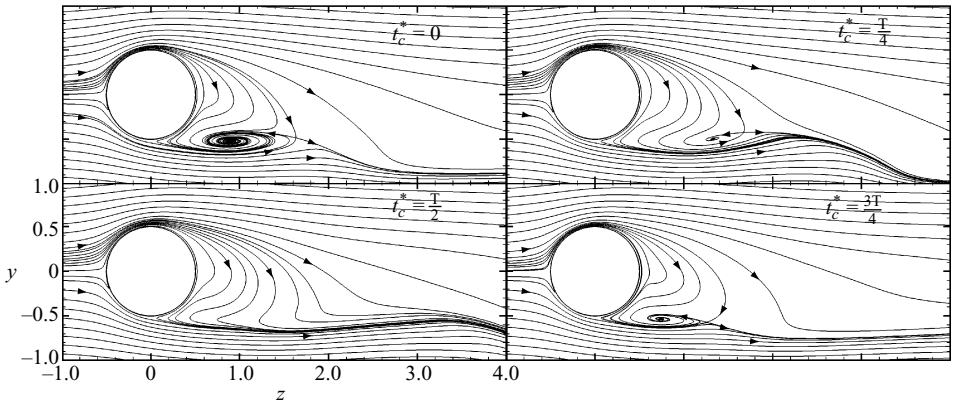


FIGURE 9. Streamline evolution on the (y, z)-plane for $Re = 250$ and $\Omega^* = 0.20$.

around the lower focus is also reduced in size for $\Omega^* \leqslant 0.08$, while at $\Omega^* = 0.10$ it undergoes a sudden growth that also marks the onset of vortex shedding. Although vortical structures are continually being shed and convected downstream, spiralling motion is only visible in the near wake, where the convection velocity is small. Further downstream, spiralling motions only become visible in a frame of reference translating at the local flow velocity. At $\Omega^* = 0.20$ the circulation region around the lower focus is larger still, while the upper focus is absent. It is under these conditions that the expansion of the wake and the oscillatory amplitude of the force coefficient histories are found to be at their maximum. For $\Omega^* \geqslant 0.30$, there are no spiralling structures in the wake, and fluid passing over the lee side of the sphere appears to stay attached until it meets fluid passing over the advancing side of the sphere and is 'peeled' away from the surface. This transition in the near-wake topology coincides with the onset of vortex shedding suppression observed in the vortical wake structure presented in figure 7.

A time sequence of the instantaneous streamline evolution on the (y, z)-plane at $\Omega^* = 0.20$ is presented in figure 9. Starting at the time instant at which the lift force is at a local minimum, the streamline pattern is presented at every quarter period, for one period (T). Fluid instantaneously entrained into the wake from the retreating side is drawn down towards the advancing side of the sphere in a stream contracting towards the flow symmetry plane. On meeting fluid passing over the advancing side of the sphere, the fluid turns back on itself and is channelled towards the centre of the lower stable focus. The fluid is then expelled normal to the symmetry plane and spirals the wake before being convected downstream. At the next quarter cycle the lower focus is displaced downstream and appears smaller. At $t_c^* = T/2$ the lower focus has detached from the near wake and is convecting downstream. In a reference frame fixed to the sphere it loses its spiral appearance. Fluid encircling the upper focus is drawn down to meet fluid passing over the advancing side and forms a shear layer. At this point, the lift coefficient attains a local maximum, and the drag coefficient is in the vicinity of a local minimum. The time $t_c^* = 3T/4$ marks the 'birth' of a new lower focus that sits closer to the sphere surface than a mature structure. Overall, the shedding cycle is one of 'build-up and release' of the region of circulation around the lower focus. Although not shown, a similar cycle is found for other rotation rates at which vortex shedding prevails.

https://doi.org/10.1017/S0022112008004655 Published online by Cambridge University Press

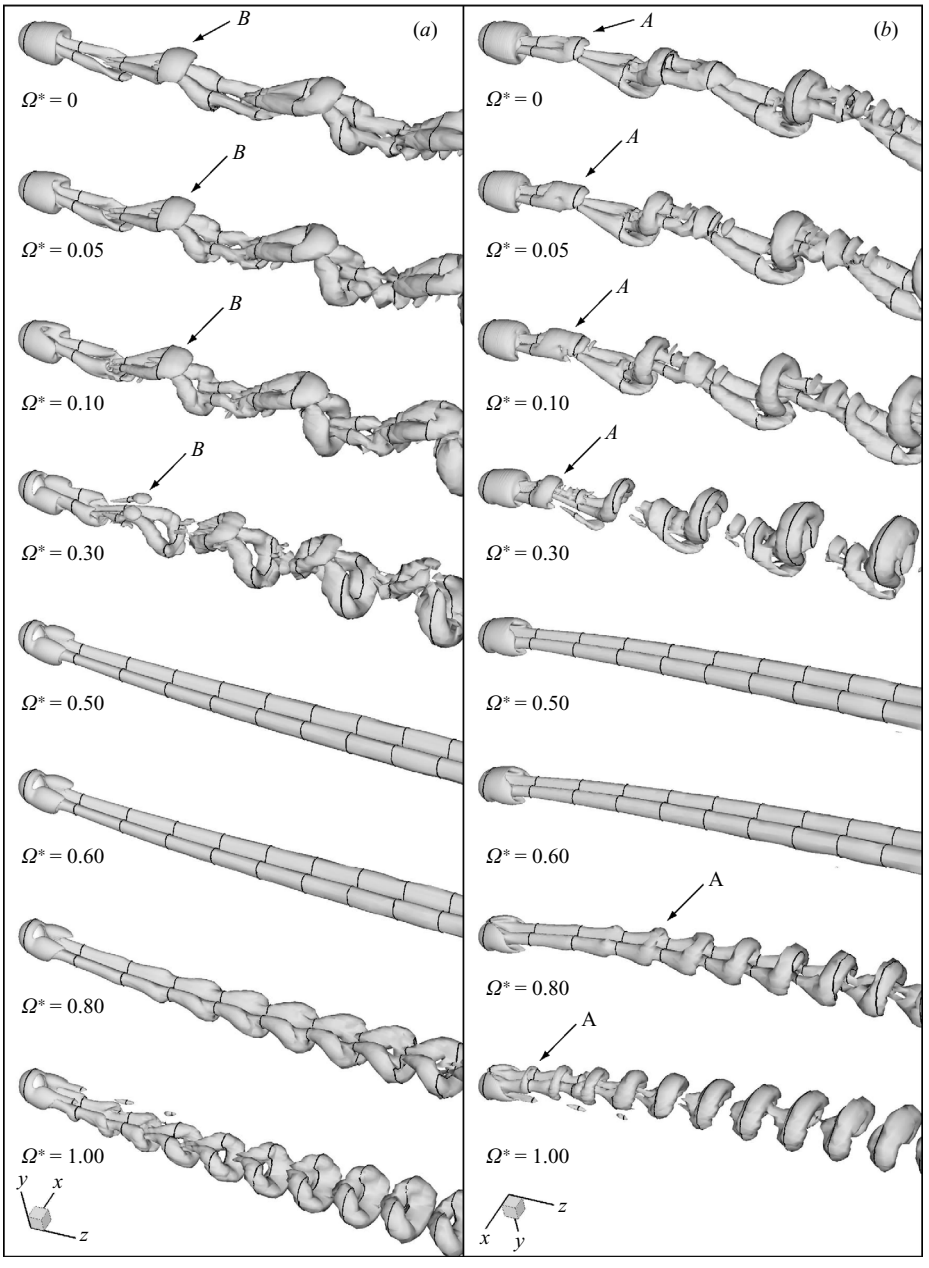


FIGURE 10. Instantaneous vortical structures for $Re = 300$: (*a*) and (*b*) look down on the wake from the retreating and advancing side of the sphere, respectively.

3.3. $Re = 300$

The effect of sphere rotation on the flow structure at $Re = 300$ is presented in figure 10. The wake undergoes a number of interesting topological transitions over the range of Ω^* considered. With increasing Ω^*, the distance between successive wake structures is progressively reduced, indicating an increase in the vortex shedding Strouhal number. The size of the induced vortices (labelled B) becomes progressively smaller in relation

https://doi.org/10.1017/S0022112008004655 Published online by Cambridge University Press

to the primary structures (labelled A) shed from the sphere. The expansion of the wake in the y-direction initially increases with the rotation rate before decreasing until the vortex shedding is suppressed in the range $0.50 < \Omega^* < 0.60$, when the wake reverts to a steady double thread. This transition is also observed at $Re = 250$ but at a slightly lower value of Ω^*. In this case however, for $\Omega^* > 0.60$, the wake undergoes a further transition to a second vortex shedding regime, which to the authors' knowledge has not previously been reported for a sphere. For a two-dimensional cylinder at $Re = 200$, Mittal & Kumar (2003) found vortex shedding to be suppressed for $\Omega^* \geqslant 1.91$ and to resume for $\Omega^* \approx 4.4$ to 4.8. It is not clear why vortex shedding is suppressed and resumes at a significantly higher rotation rate for a two-dimensional cylinder.

In the second vortex shedding regime, the wake shows a distinctly different topology, and the process by which discrete vortical structures are formed and released downstream appears to be different, suggesting that a different mechanism is driving the unsteadiness. At $\Omega^* = 0.80$, the vortex shedding does not originate in the near wake of the sphere, as is the case at lower Ω^*. The double-threaded structure extends some distance downstream from the sphere before waviness is observed in the threads; the threads then tilt and connect to form a compact series of hairpin structures. As the wake convects downstream, the hairpins are tilted away from the streamwise direction and assume a more distinct Ω shape. This wake development resembles the buoyant coflowing wake studied by Perry & Lim (1978) and Perry & Tan (1984). Oblique Kelvin–Helmholtz-like instabilities develop in the cylindrical vortex sheet, causing it to develop folds which lead to the formation of one-sided structures that resemble a daisy chain of interlocking loops. At $\Omega^* = 1.00$, the formation of the hairpin structures occurs further upstream; otherwise, the flow topology is similar to that at $\Omega^* = 0.80$. It is interesting to note that this second transition to a vortex shedding regime does not occur for $Re = 250$ and $\Omega^* \leqslant 1.00$, despite the similarities in the flow structure at lower Ω^*. This raises the question of whether at lower Reynolds numbers, the transition to the second vortex shedding regime is triggered at a higher value of Ω^*. To test this possibility further simulations need to be conducted for $\Omega^* > 1.00$.

Figure 11 shows the near-wake streamline patterns on the (y, z)-plane for $Re = 300$ and a number of representative rotation rates. For a stationary sphere, the instantaneous streamlines resemble those for a stationary sphere at $Re = 250$. The most noticeable difference is that the region of circulation around the lower focus is larger and sits closer to the sphere. With increasing rotation rate the recirculating wake region is progressively reduced in a fashion similar to that found for $Re = 250$. For $\Omega^* \geqslant 0.30$, all spiralling structures in the wake are absent, and the flow appears to remain attached to the surface. The progressive reduction in the circulating wake volume with increasing rotation rate may explain the increase in the vortex shedding frequency. Intuitively, the build-up and concentration of vorticity should occur at a faster rate as the volume of the recirculating region is reduced. An increase in the entrainment of free stream fluid may also drive the shedding cycle at a faster rate.

As the rotation rate is increased further, the fluid passing over the retreating side of the sphere becomes increasingly vectored in the negative y-direction. Despite the transition to a second vortex shedding regime for $\Omega^* \geqslant 0.80$, the streamline pattern is topologically unchanged. Unlike the shedding cycle at lower rotation rates, here the shedding mechanism is clearly not one of 'build-up and release' of vortical structures from the near wake. Although unsteady spiralling structures exist further downstream, in a reference frame translating with the sphere they appear merely as a waviness in the downstream streamlines. To reveal the wake structures (as identified

https://doi.org/10.1017/S0022112008004655 Published online by Cambridge University Press

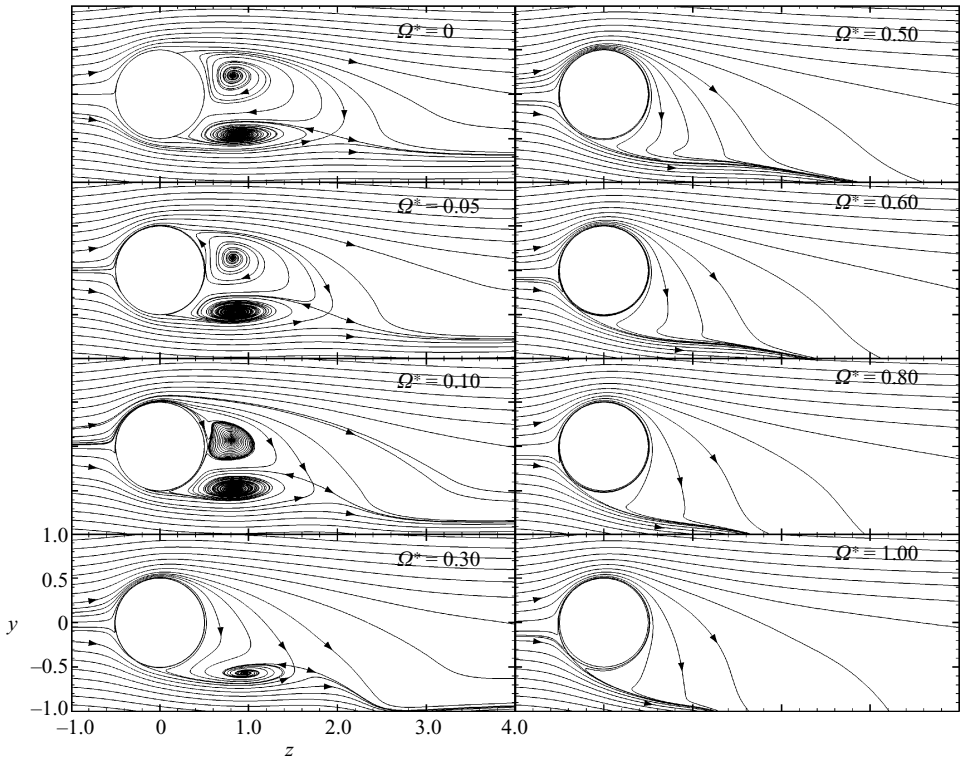


FIGURE 11. Instantaneous near-wake streamline patterns on the (y, z)-plane for $Re = 300$.

in figure 10), the velocity field must be viewed relative to an observer moving close to their convection velocity. For a wake flow, the structures develop with streamwise extent and are not periodic in space; therefore a unique convection velocity does not, in general, exist. In figure 12 the instantaneous streamline pattern for $\Omega^* = 0.80$ is overlayed with greyscale contours of λ_2. The velocity of the observer was chosen as the convection velocity of the vortical structure centred at $(x, y, z) = (0, -2.378, 11.554)$, at which point the local velocity is $(u_x, u_y, u_z) = (0, -0.093, 0.821)$. The centre of the structure was assumed to coincide with the local minimum in λ_2.

In this chosen reference frame, the streamline pattern reveals a vortex sheet curling up into a series of stable foci that are separated by saddles. The locations of the foci coincide with the locations at which the hairpin structures, as identified by the λ_2 definition, intersect the symmetry plane. With downstream distance, the waviness in the vortex sheet grows until fluid is observed to roll up into foci. At the time instant shown the initial roll-up of the shear layer is evident near $z = 5.0$. As the focal structures are convected downstream they grow and entrain more of the surrounding fluid.

Above the chain of stable foci, a positive open bifurcation line exists from which streamlines on either side diverge. The downstream streamline pattern bears a striking resemblance to the phase-averaged streamline patterns presented by Perry, Lim & Chong (1980) and Perry & Tan (1984) for a negatively buoyant wake. From continuity arguments, fluid entrained into the stable foci is ejected from either side of the symmetry plane, while fluid must converge towards the positive open bifurcation line from either side of the symmetry plane. Although the experiments of Perry *et al.*

https://doi.org/10.1017/S0022112008004655 Published online by Cambridge University Press

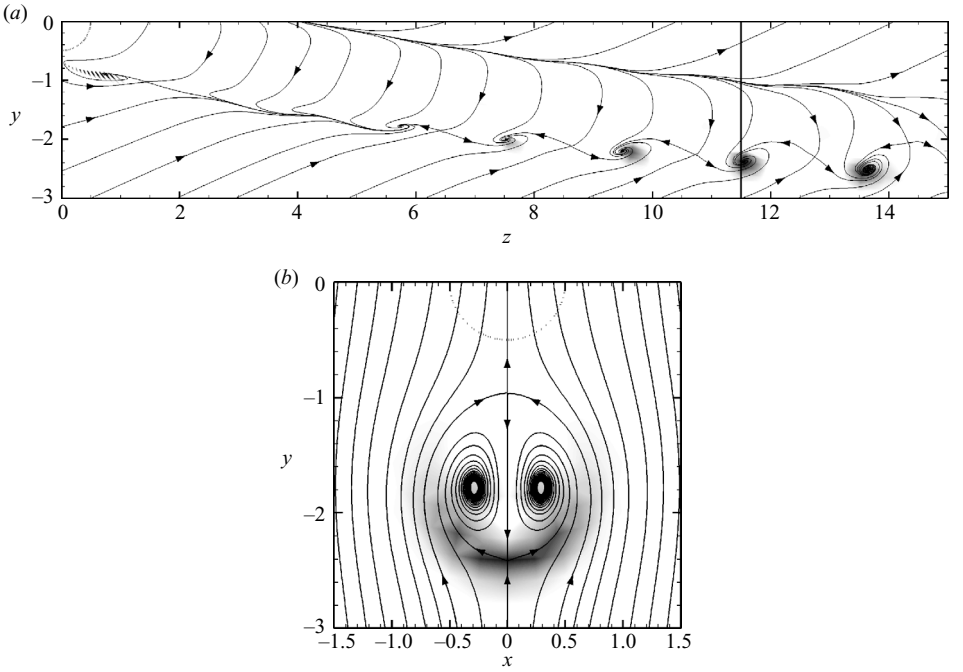


FIGURE 12. Instantaneous streamline pattern for $Re = 300$ and $\Omega^* = 0.80$: (*a*) (y, z)-plane; (*b*) cross-stream plane at $z = 11.5$. The observer is moving at $(u_x, u_y, u_z) = (0, -0.093, 0.821)$. Patterns are overlayed with greyscale contours of λ_2 in the range -0.0008 to -0.34. The sphere outline is indicated by a dashed line centred at the origin.

(1980) were limited to field measurements on the flow symmetry plane, continuity arguments allowed them to conjecture the streamline pattern in a cross-flow plane. Figure 12(*b*) shows the streamline pattern computed from the in-plane velocity vectors projected onto the cross-flow plane at $z = 11.5$, together with the contours of λ_2. The plane of interest is indicated in figure 12(*a*). The computed streamline pattern is in agreement with those conjectured by Perry *et al.* (1980). The bifurcation line apparent on the symmetry plane forms part of a stream surface, which in the cross-flow plane, appears as a separatrix streamline. The cross-stream pattern is characterized by a pair of counter-rotating foci which entrain fluid from below the separatrix streamline and produce a downwash on the symmetry plane. The cross-flow plane cuts through the head of a hairpin structure, and as a result the contours of λ_2 take a kidney shape. The streamline pattern is consistent with the formation of trailing vortices.

To gain further insight into the process driving the second transition, figure 13 presents the instantaneous vorticity field on the (y, z)-plane. Since the (y, z)-plane coincides with the flow symmetry plane only the x-vorticity component is non-zero. Contours range from -20 to 20 in increments of 0.5, with the dashed lines used to indicate negative values and the zero contour omitted for clarity. For a stationary sphere, the shear layer separating from the lower side of the sphere is more intense, and it is from this side – where vorticity is most concentrated – that vorticity is periodically discharged downstream. The presence of the toroidal wake, as identified in the near-wake streamline patterns, is not apparent in the vorticity contours. Vorticity fails to distinguish between rotation resulting from a swirling motion and rotation due to

https://doi.org/10.1017/S0022112008004655 Published online by Cambridge University Press

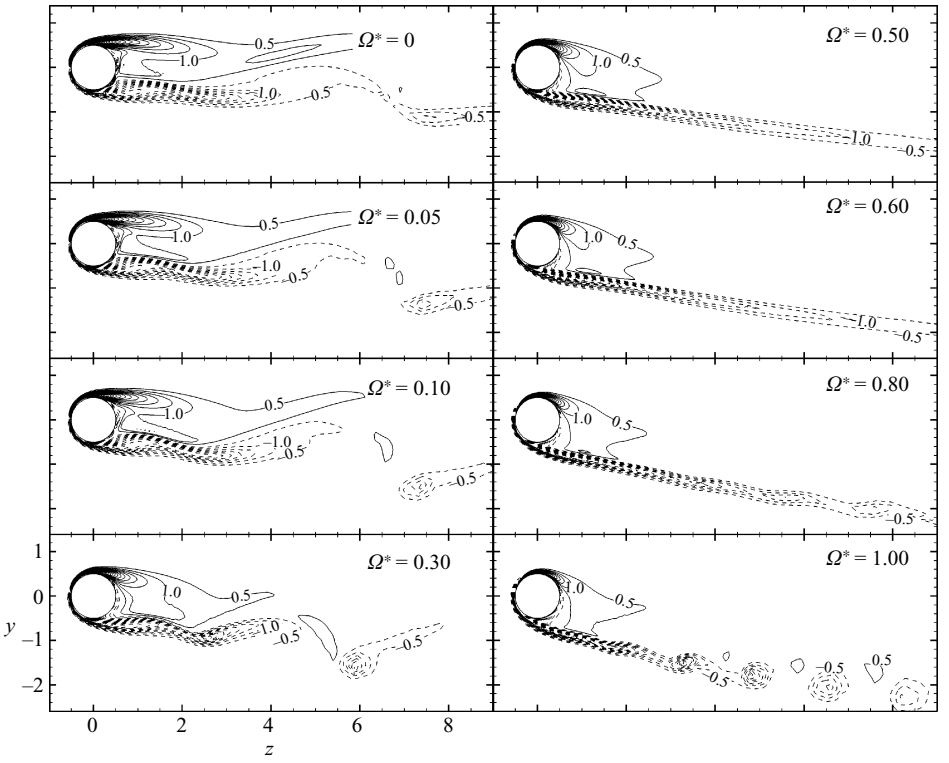


FIGURE 13. Contours of instantaneous x-vorticity on the (y, z)-plane for $Re = 300$.

shear, and here the cylindrical shear layer released from the surface is of a sufficient magnitude to mask the details of the toroidal near wake.

The introduction of sphere rotation increases the surface-to-free stream velocity gradient over the advancing side of the sphere and decreases it over the retreating side. This leads to a progressive intensification and thinning of the shear layer released from the advancing side. As a result, the patches of negative vorticity which are periodically discharged downstream are noticeably stronger. The shear layer over the retreating side is weakened and retracts upstream with increasing rotation rate. It also expands in the y-direction and is drawn down over the lee side of the sphere. The effect is most pronounced on the (y, z)-plane in which the sphere's peripheral velocity is greatest.

For $\Omega^* \geqslant 0.50$, the wake reverts to a steady state, and the vorticity field, on the plane, is characterized by a thin shear layer separating from the advancing side of the sphere. At $\Omega^* = 0.80$, the shear layer separating from the advancing side shows some waviness, and this precedes it rolling up to form a series of concentrated vorticity patches. At the time instant shown, these patches occur near $z = 5.5$ and $z = 7.5$ and coincide with the locations at which shed hairpin structures intersect the symmetry plane. Unlike the structures shed at lower rotation rates, which appear to scale with the diameter of the sphere, these structures scale with the thickness of the shear layer. For $\Omega^* = 1.00$, the roll-up of the shear layer occurs further upstream, and the patches of vorticity released downstream are stronger. As these structures propagate downstream they grow and become more diffused. This second transition to vortex shedding works to redistribute the shear layer vorticity, which becomes

https://doi.org/10.1017/S0022112008004655 Published online by Cambridge University Press

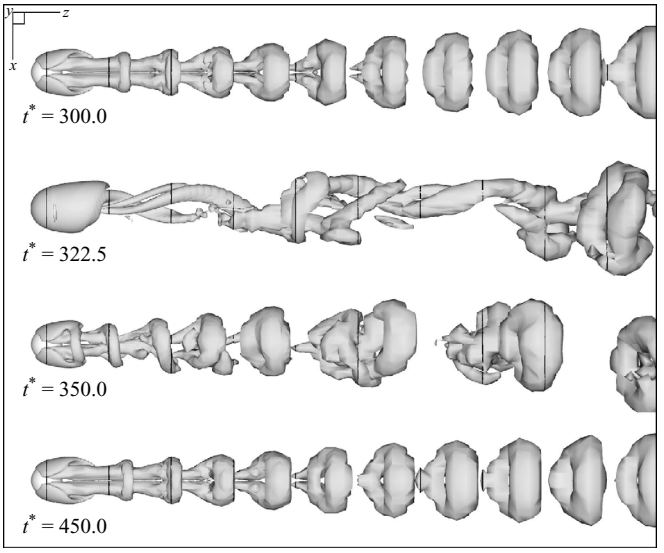


FIGURE 14. Effect of symmetry breaking perturbation for $Re = 300$ and $\Omega^* = 1.00$. The time sequence begins with the statistically steady flow for transversely rotating sphere at $t^* = 300.0$. This is followed by streamwise rotation for $300.0 < t^* \leqslant 322.5$ and transverse rotation for $t^* > 322.5$. Vortical structures are identified by plotting isosurfaces of $\lambda_2 = -8 \times 10^{-4}$.

increasingly concentrated as the rotation rate and Reynolds number are increased. These features combine to suggest that the mechanism driving the unsteadiness is a Kelvin–Helmholtz instability of the shear layer separating from the advancing side of the sphere.

Over the Reynolds number and rotation rates tested, the wake maintains a planar symmetry normal to the sphere rotation axis. To verify that this symmetry plane is physical and not an artefact of the numerical method, a number of symmetry-breaking perturbations were introduced. Figure 14 illustrates a symmetry-breaking test applied to the case of $Re = 300$ and $\Omega^* = 1.00$. The highest Reynolds number simulated is presented here because it is expected to be the most sensitive to symmetry-breaking perturbations. The time sequence begins with the statistically steady flow for a transversely rotating sphere at non-dimensional time $t^* = 300.0$, followed by an impulsive change to streamwise rotation for $300.0 < t^* < 332.5$. This gross perturbation breaks the planar symmetry, and structures spiral about the streamwise axis as they are convected downstream, in a fashion similar to the wake structures computed by Kim & Choi (2002) for a sphere undergoing steady streamwise rotation. Once rotation in the transverse sense is impulsively restored at $t^* = 332.5$, the wake symmetry plane is quickly re-established without hysteresis. Quantitatively, the symmetry of the wake can be ascertained by monitoring the zeroth azimuthal mode of u_ϕ. The zeroth azimuthal mode $\widehat{u_\phi}(k = 0)$ can be regarded as the average azimuthal velocity and should be zero if planar symmetry exists. Figure 15 presents the time history of $\widehat{u_\phi}(k = 0)$ at two stations in the wake, and it illustrates that once transverse rotation is restored the symmetry plane is re-established. Such tests have indicated that the flow symmetry plane is physical.

3.4. *Force coefficients*

In the modelling of particulate flows the forces experienced by a particle are of interest. The time-averaged total, pressure and viscous components of the drag coefficient, $\overline{C_D}$,

https://doi.org/10.1017/S0022112008004655 Published online by Cambridge University Press

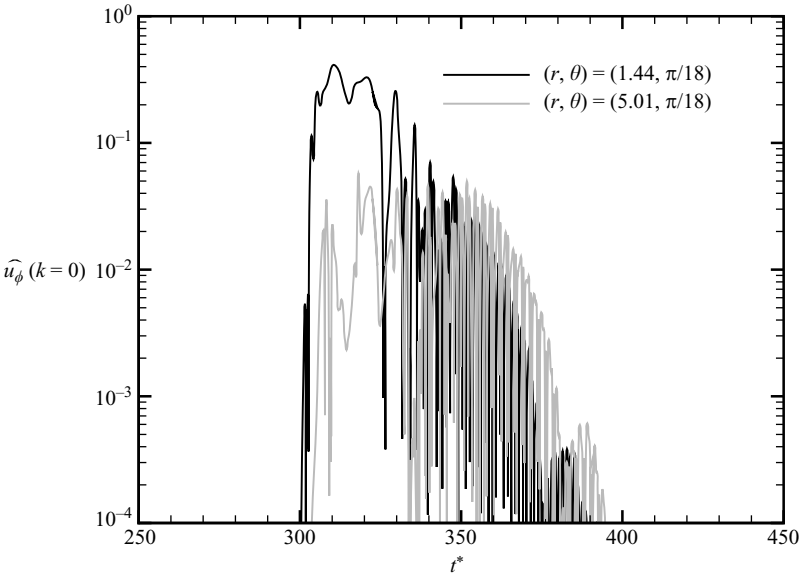


FIGURE 15. Time history of azimuthal mode $k = 0$ of u_ϕ at $(r, \theta) = (1.51, \pi/18)$ and $(6.10, \pi/18)$.

and lift coefficient, $\overline{C_{Ly}}$, are presented versus Ω^* in figures 16 and 17; $\overline{C_{Lx}}$ is omitted because the flow maintains a symmetry about the (y, z)-plane for all cases considered and is therefore identically zero. Also presented are the total values computed by Kurose & Komori (1999) for $Re = 100$ and $Re = 300$ and Niazmand & Renksizbulut (2003) for $Re = 100$, 250 and 300.

For all three Reynolds numbers the viscous component of $\overline{C_D}$ remains relatively constant with increasing Ω^*, while the pressure component sees a gradual increase. With increasing Reynolds number the total drag is reduced, while the pressure component comprises a greater percentage of the total drag coefficient. For $Re = 250$ and $Re = 300$, the drag coefficients computed by Kurose & Komori (1999) and Niazmand & Renksizbulut (2003) show good agreement with the present study, while for $Re = 100$ these studies predict lower values. Good agreement for $\overline{C_{Ly}}$ is found only in the vicinity of $\Omega^* = 0$. With increasing Ω^*, the current study predicts increasingly higher values of the $\overline{C_{Ly}}$.

The peak-to-peak fluctuating components of the drag coefficient, ΔC_D, and lift coefficient, ΔC_{Ly}, are shown in figure 18. With increasing Ω^* both ΔC_D and ΔC_{Ly} increase towards a maximum in the vicinity $\Omega^* = 0.20$, before decreasing to zero for $\Omega^* > 0.30$. This increase and subsequent decrease in the oscillatory amplitudes coincides with the expansion and contraction of the wake structures presented in §§ 3.2 and 3.3. For both Reynolds numbers, ΔC_{Ly} attains a maximum which is approximately a factor of four greater than ΔC_D. Both ΔC_{Ly} and ΔC_D attain maxima which increase by approximately a factor of two between $Re = 250$ and $Re = 300$. At $Re = 300$, the force coefficients also undergo small periodic oscillations for $\Omega \geqslant 0.80$, with the amplitude increasing at $\Omega^* = 1.00$. In the previous section it was found that in the second vortex shedding regime, the near wake resembles that at lower rotation rates, where the wake is steady. The lack of activity in the near wake explains these relatively low-amplitude oscillations in this second shedding regime.

https://doi.org/10.1017/S0022112008004655 Published online by Cambridge University Press

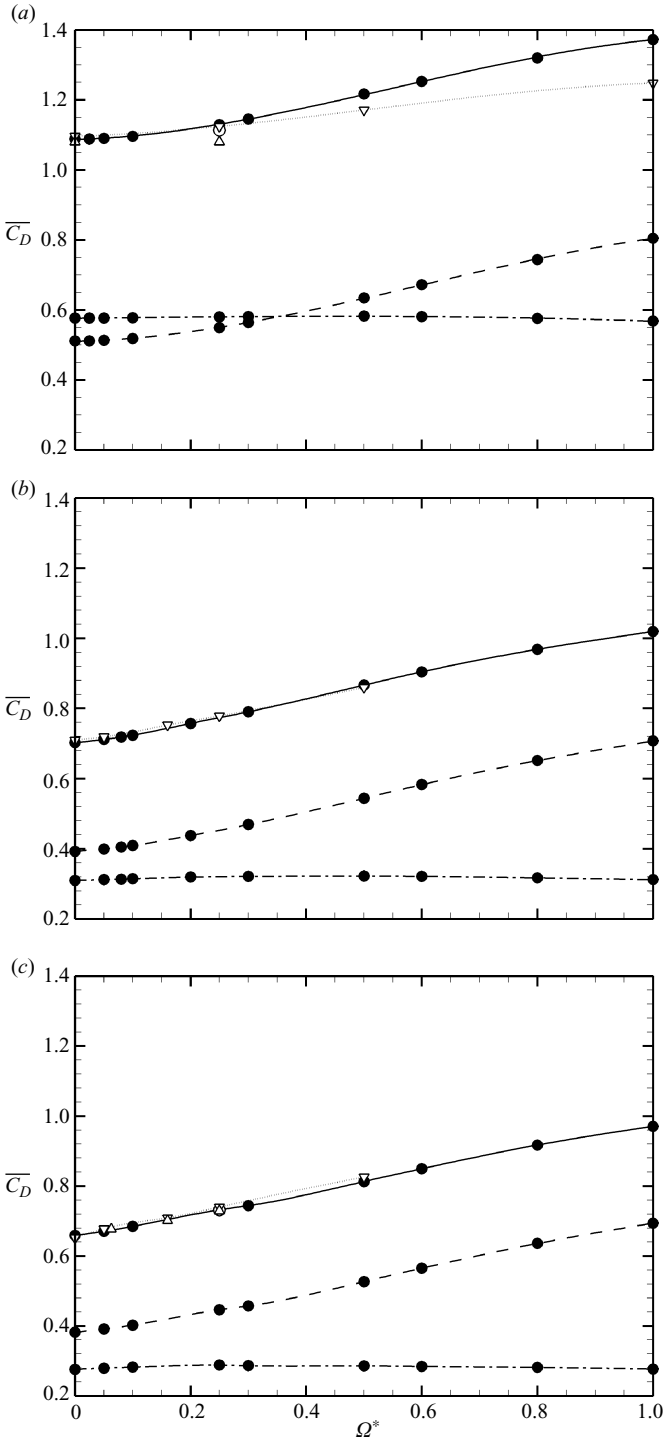


FIGURE 16. Time-averaged drag coefficient, $\overline{C_D}$, versus Ω^*: (*a*) $Re = 100$; (*b*) $Re = 250$; (*c*) $Re = 300$. Present study: —●— total; — ● — pressure component; –·–●–·– viscous component. △ Kurose & Komori (1999); ·····▽····· Niazmand & Renksizbulut (2003); ○ present study using the boundary conditions of Kurose & Komori (1999).

https://doi.org/10.1017/S0022112008004655 Published online by Cambridge University Press

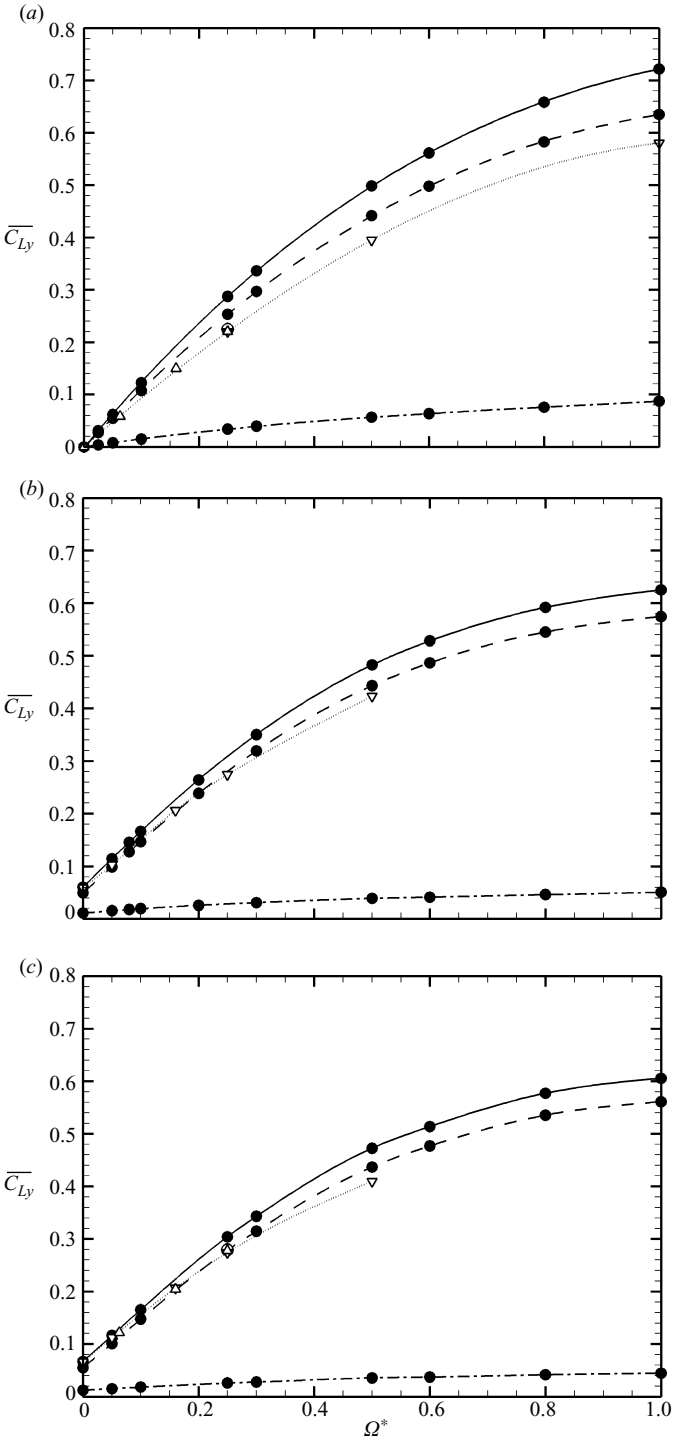


FIGURE 17. Time-averaged lift coefficient, $\overline{C_{Ly}}$, versus Ω^*: (*a*) $Re = 100$; (*b*) $Re = 250$; (*c*) $Re = 300$. Present study: —●— total; — ● — pressure component; -·-●-·- viscous component. △ Kurose & Komori (1999); ·····▽····· Niazmand & Renksizbulut (2003); ○ present study using the boundary conditions of Kurose & Komori (1999).

https://doi.org/10.1017/S0022112008004655 Published online by Cambridge University Press

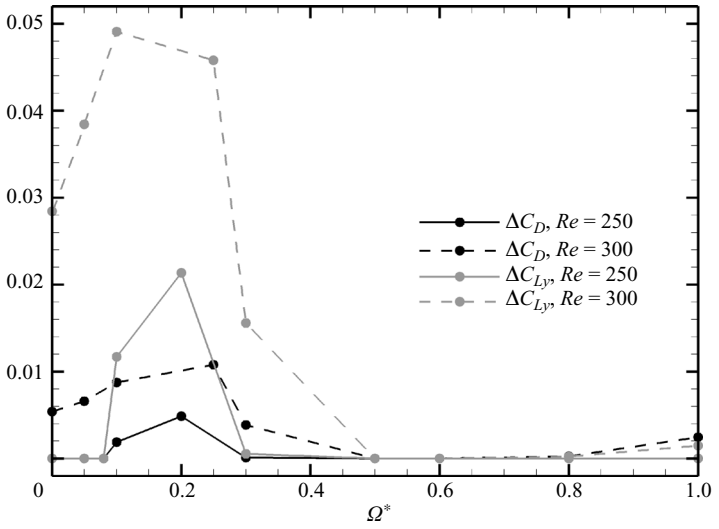


FIGURE 18. Peak-to-peak oscillatory amplitude of the drag coefficient, ΔC_D, and lift coefficient, ΔC_{Ly}.

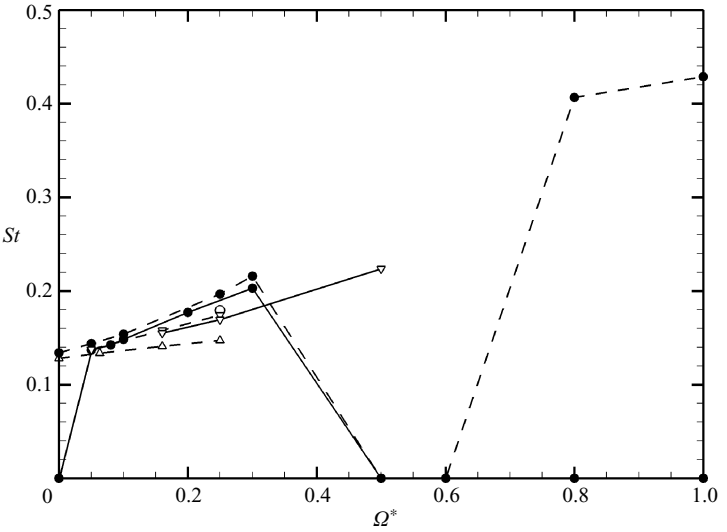


FIGURE 19. Vortex shedding Strouhal number, St, versus Ω^*: —●— present study at $Re = 250$; — • — present study at $Re = 300$; ○, present study at $Re = 300$, using the boundary conditions of Kurose & Komori (1999); —▽— Niazmand & Renksizbulut (2003) at $Re = 250$; — ▽ — Niazmand & Renksizbulut (2003) at $Re = 300$; — △ — Kurose & Komori (1999) at $Re = 300$.

It was inferred from the wake structures presented in § 3.3 that the dominant frequency of oscillation increases with Ω^*. Figure 19 presents the vortex shedding Strouhal number, St, versus Ω^* for $Re = 250$ and $Re = 300$; St was computed from the power spectrum of the C_D and C_{Ly} time histories. For $Re = 250$ and $\Omega^* = 0.05$ and 0.08, the amplitude of oscillation decays; so St is estimated by directly measuring the period of oscillation from the transient solution. The St, shows a relatively linear increase with Ω^*, particularly for values of Ω^* below the onset of wake shedding

https://doi.org/10.1017/S0022112008004655 Published online by Cambridge University Press

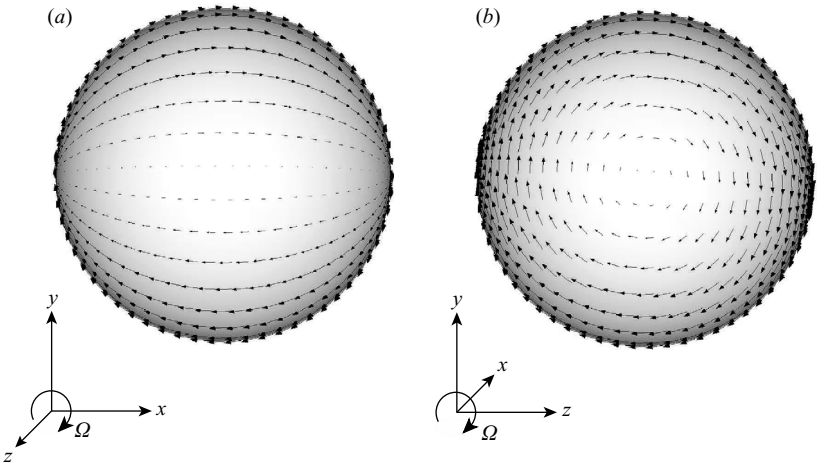


FIGURE 20. Velocity vectors on the surface of the sphere: (*a*) boundary condition implemented by Kurose & Komori (1999) and Niazmand & Renksizbulut (2003); (*b*) boundary condition implemented in the present study. The axis of rotation is normal to the page.

suppression. Although the flow, in the absence of rotation, is significantly different for the two Reynolds numbers, the effect of rotation drives vortex shedding at a similar frequency. Also shown in figure 19 are the shedding frequencies computed in the studies of Kurose & Komori (1999) and Niazmand & Renksizbulut (2003).† Good agreement is found only at low Ω^*, while the present study predicts an increasingly higher shedding frequency as Ω^* increases.

The discrepancy in the Strouhal number and the time-averaged force coefficients presented earlier appears to be a result of differences in the velocity boundary condition at the surface of the spinning sphere. Figure 20 compares the velocity vectors on the surface of the sphere derived from the boundary condition defined by (2.12)–(2.14) of Kurose & Komori (1999) and the boundary condition used in the present study (2.5). In a cylindrical coordinate system (r, ϕ, z) the present boundary condition at the sphere surface (2.5) can be expressed as

$$\boldsymbol{u}_s = -\frac{\Omega d}{2}(\sin\phi\cos\theta\widehat{\boldsymbol{e}}_{\boldsymbol{r}} + \cos\phi\cos\theta\widehat{\boldsymbol{e}}_{\boldsymbol{\phi}} - \sin\theta\sin\phi\widehat{\boldsymbol{e}}_{\boldsymbol{z}}). \tag{3.1}$$

By transforming the surface velocity profile in figure 20(*a*) into the coordinate system used in this study, it becomes evident that it is the ϕ-component of (3.1) that has been ignored. The resultant velocity boundary condition generates less circulation for a given Ω^* and explains the lower lift force coefficient, drag force coefficient and Strouhal number predicted by Kurose & Komori (1999) and Niazmand & Renksizbulut (2003). The lower circulation is also expected to delay vortex suppression to higher Ω^* and explains why Niazmand & Renksizbulut (2003) observed a sustained periodic vortex shedding for $Re = 250$ and $\Omega^* = 0.5$, while Best (1998) and the present study have found vortex shedding to be suppressed under these conditions. You *et al.* (2003) also alluded to this problem. For $Re = 1.0$ they found the lift coefficient to be close to the value theoretically derived by Rubinow & Keller (1961) and noted that Kurose & Komori (1999) reported a much lower value. For $Re = 68.4$ and $\Omega^* = 1.0$,

† Niazmand & Renksizbulut (2003) do not present *St*, and so the shedding frequency is estimated by measuring the period of oscillation from the lift coefficient histories.

https://doi.org/10.1017/S0022112008004655 Published online by Cambridge University Press

You *et al.* (2003) reported a lift coefficient of 0.79 and a drag coefficient of 1.73. Good agreement is found with the present study, which finds a lift coefficient of 0.77 and a drag coefficient of 1.73.

The boundary condition used by Kurose & Komori (1999) and Niazmand & Renksizbulut (2003) was introduced into the solver used in the present study and tested for $\Omega^* = 0.25$ and $Re = 100$ and 300. The force coefficients computed for these cases are included in figures 16 and 17, while the vortex shedding Strouhal number for $Re = 300$ and $\Omega^* = 0.25$ is included in figure 19. For both Reynolds numbers good agreement is found between the force coefficients derived from these simulations and the values computed by Kurose & Komori (1999) and Niazmand & Renksizbulut (2003). Good agreement is also found between the Strouhal number derived for $Re = 300$ and $\Omega^* = 0.25$ and the value computed by Niazmand & Renksizbulut (2003).

4. Summary and concluding remarks

The uniform flow past a sphere in steady transverse rotation is studied numerically for the Reynolds numbers 100, 250 and 300. The primary objective was to reveal the structure of the wake flow over the range of rotational speeds $\Omega^* = 0.00$ to 1.00, where Ω^* is the maximum velocity on the sphere surface normalized by the free stream velocity.

As the rotation rate is increased, the relative free stream-to-surface velocity is increased on the advancing side of the sphere and decreased on the retreating side. As a result, free stream fluid becomes increasingly vectored over the lee side of the sphere, and the volume of the recirculating region is progressively reduced until it is completely destroyed for rotation rates higher than $\Omega^* = 0.30$ to 0.50. On the advancing side the higher relative velocity leads to a progressive intensification of the shear layer separating from this side of the sphere. These processes have different effects on the global wake structure, depending on the Reynolds number.

At $Re = 100$ the initially axisymmetric wake undergoes a transition to a double-threaded structure. As the rotation rate is increased a greater circulation is generated, which leads to the intensification of the threads. However, the flow remains steady. At $Re = 250$ sphere rotation triggers a transition to a vortex shedding regime characterized by the shedding of vortex loops at a single shedding frequency. Vortex shedding is often described as a process of 'build-up and release' of the fluid within the recirculating wake. As the wake is reduced in volume, this process must occur on a faster time scale, such that the vortex shedding Strouhal number increases. At higher rotation rates, the recirculating wake is completely absent, and the conditions necessary for vortex shedding are eliminated. The wake then resembles the double-threaded structure found at $Re = 100$.

At $Re = 300$ the wake of a stationary sphere is unsteady. As the rotation rate is increased beyond a critical value, vortex shedding is suppressed via the same mechanism found for $Re = 250$. In this case, the shedding of vortical structures returns for $\Omega^* \geqslant 0.80$ albeit in a different form. Unlike the shedding process at lower rotation rates, the discrete vortical structures originate from the roll-up of vorticity along the intense shear layer separating from the advancing side of the sphere. The absence of such an instability at lower Reynolds numbers is congruent with the instability mechanism being of the Kelvin–Helmholtz type. To the authors' knowledge, this second transition has never been observed before. These findings provide important

https://doi.org/10.1017/S0022112008004655 Published online by Cambridge University Press

information towards understanding the process of turbulence enhancement resulting from the presence of solid particles in a fluid.

The simulation of particulate-laden flows requires an accurate description of the forces experienced by the solid particles. At moderate Reynolds numbers, accurate experimental measurements are difficult due to the small loads experienced by the sphere and the presence of supporting devices. These issues are not present in numerical simulation; however, it was discovered that previous numerical studies in the range $Re = 100$ to $Re = 300$ had incorrectly specified the boundary conditions on the sphere surface. In light of this the present study constitutes the first accurate numerical investigation of the forces experienced by a transversely rotating sphere in the Reynolds number range 100 to 300.

The material presented draws on work completed at the University of Melbourne as part of the PhD thesis of M. Giacobello. M. Giacobello would like to acknowledge the support of J. Drobik of the Defence Science and Technology Organisation (DSTO) for this work. The authors would like to acknowledge the many useful suggestions received from Professor M. S. Chong on this work. Thanks also go to Professor K. Dongjoo and Professor H. Choi for providing data used in the validation of the code. The authors would also like to express their gratitude to the Victorian Partnership for Advanced Computing (VPAC) and Australian Partnership for Advanced Computing (APAC) for providing the computing resource necessary in this study.

REFERENCES

Bagchi, P. & Balachandar, S. 2002 Steady planar straining flow past a rigid sphere at moderate Reynolds number. *J. Fluid Mech.* **466**, 365–407.

Bagchi, P. & Balachandar, S. 2003 Effect of turbulence on the drag and lift of a particle. *Phys. Fluids* **15** (11), 3496–3513.

Best, J. L. 1998 The influence of particle rotation on wake stability at particle Reynolds numbers, $Re_P < 300$; implications for turbulence modulation in two-phase flows. *Intl. J. Multiphase Flow* **24**, 693–720.

Constantinescu, G. S. & Squires, K. D. 2000 LES and DNS investigation of turbulent flow over a sphere. *AIAA Paper* 2000-0540.

Giacobello, M. 2005 Wake structure of a transversely rotating sphere at moderate Reynolds numbers. PhD thesis, University of Melbourne, Melbourne, VIC, Australia.

Jeong, J. & Hussain, F. 1995 On the identification of a vortex. *J. Fluid Mech.* **285**, 69–94.

Johnson, T. A. & Patel, V. C. 1999 Flow past a sphere up to a Reynolds number of 300. *J. Fluid Mech.* **378**, 19–70.

Kim, D. & Choi, H. 2002 Laminar flow past a sphere rotating in the streamwise direction. *J. Fluid Mech.* **461**, 365–386.

Kim, J. & Moin, P. 1985 Application of a fractional-step method to incompressible Navier–Stokes equations. *J. Comp. Phys.* **59**, 308–323.

Kurose, R. & Komori, S. 1999 Drag and lift forces on a rotating sphere in a linear shear flow. *J. Fluid Mech.* **384**, 183–206.

Maccoll, J. H. 1928 Aerodynamics of a spinning sphere. *J. Roy. Aero. Soc.* **32**, 777–798.

Mittal, R. 1999 A Fourier–Chebyshev collocation method for simulating flow past spheres and spheroids. *Int. J. Numer. Meth. Fluids* **30**, 921–937.

Mittal, S. & Kumar, B. 2003 Flow past a rotating cylinder. *J. Fluid Mech.* **476**, 303–334.

Nakamura, I. 1976 Steady wake behind a sphere. *Phys. Fluids* **19** (1), 5–8.

Niazmand, H. & Renksizbulut, M. 2003 Surface effects on transient three-dimensional flows around rotating spheres at moderate Reynolds numbers. *Comput. Fluids* **32**, 1405–1433.

Oesterlé, B. & Dinh, B. 1998 Experiments on the lift of a spinning sphere in a range of intermediate Reynolds numbers. *Exps. Fluids* **25**, 16–22.

https://doi.org/10.1017/S0022112008004655 Published online by Cambridge University Press

Pan, Y., Tanaka, T. & Tsuji, Y. 2001 Direct numerical simulation of particle-laden rotating turbulent channel flow. *J. Fluid Mech.* **13** (8), 222–230.

Perry, A. E. & Lim, T. T. 1978 Coherent structures in coflowing jets and wakes. *J. Fluid Mech.* **88** (3), 451–463.

Perry, A. E., Lim, T. T. & Chong, M. S. 1980 The instantaneous velocity fields of coherent structures in coflowing jets and wakes. *J. Fluid Mech.* **101** (2), 243–256.

Perry, A. E. & Tan, D. K. M. 1984 Simple three-dimensional vortex motions in coflowing jets and wakes. *J. Fluid Mech.* **141**, 197–231.

Rubinow, S. I. & Keller, J. B. 1961 The transverse force on a spinning sphere moving in a viscous fluid. *J. Fluid Mech.* **11**, 447–459.

Steiner, T. R. 1984 A study of turbulent wakes and the vortex formation process. PhD thesis, University of Melbourne, Melbourne, VIC, Australia.

Taneda, S. 1956 Experimental investigation of the wake behind a sphere at low Reynolds numbers. *J. Phys. Soc. Jpn* **11**, 1104.

Tomboulides, A. G. & Orszag, S. A. 2000 Numerical investigation of transition and weak turbulent flow past a sphere. *J. Fluid Mech.* **416**, 45–73.

Torobin, L. B. & Gauvin, W. H. 1960 Fundamental aspects of solids-gas flow, part iv: The effects of particle rotation, roughness and shape. *Can. J. Chem. Engng.* **38**, 142–153.

Tsuji, Y., Morikawa, Y. & Mizuno, O. 1985 Experimental measurements of the Magnus force on a rotating sphere at low Reynolds numbers. *Trans. ASME* **107**, 484–488.

You, C. F., Qi, H. Y. & Xu, X. C. 2003 Lift force on rotating sphere at low Reynolds numbers and high rotational speeds. *ACTA Mech. Sin.* **19** (4), 300–307.

https://doi.org/10.1017/S0022112008004655 Published online by Cambridge University Press